Vortex Interaction in Transonic Flow for Wing-Mounted UHBR Nacelles

Spinner, Sebastian* and Rudnik, Ralf†
German Aerospace Center (DLR), Lilienthalplatz 7, 38108 Braunschweig, Germany

In this work upper wing vortices originating from the installation of a closely coupled UHBR nacelle on a long range transport aircraft are investigated under high speed flight conditions. Flow conditions at moderate angle of attack as well as high speed stall are considered. The investigations are executed by means of RANS simulations using a Reynolds stress turbulence model. It was found that a horseshoe vortex forms on the pylon leading edge at the intersection with the nacelle surface. The inboard part of the horseshoe vortex is deflected by the pressure field of the wing forcing it to pass over its suction side through the transonic flow field. A second vortex is found originating from the nacelle and passing over the wing without significantly altering the wing pressure distribution. Furthermore, for high angles of attack a strong vortex emerges from a corner separation in the pylon-wing intersection resulting in a flow separation towards the wing trailing edge.

Nomenclature

α	=	angle of attack, [°]
C_p	=	pressure coefficient, [-]
Re	=	Reynolds Number, [-]
M	=	Mach Number, [-]
ω	=	vorticity, [s^{-1}]
ω_x	=	x-vorticity, [s^{-1}]
x	=	x-coordinate, [m]
c	=	local chord, [m]
μ_t	=	turbulent viscosity, [kg m^{-1} s^{-1}]
μ_l	=	laminar viscosity, [kg m^{-1} s^{-1}]
Q	=	Q-criterion, [s^{-2}]

DFG	=	Deutsche Forschungsgemeinschaft
HGF	=	Helmholtz Gemeinschaft Deutscher Forschungszentren
ETW	=	European Transonic Wind Tunnel
DLR	=	Deutsches Zentrum für Luft und Raumfahrt
RANS	=	Reynolds Averaged Navier Stokes
PSP	=	Pressure Sensitive Paint
PIV	=	Particle Image Velocimetry
UHBR	=	Ultra High Bypass Ratio

I. Introduction

While various new propulsion concepts for civil aviation reveal a promising potential for short and medium range aircraft, no realistic alternative to the turbofan will be available for long range aircraft in the near future. Especially for environmentally compatible aviation with energy sources like hydrogen or sustainable aviation fuel, turbofan engines are expected to be utilized for future long range aircraft. In the latest generation of civil airliners, turbofan engines with a bypass ratio of up to 10 have been used. Now, ultra high bypass ratio (UHBR) engines with bypass ratios of about 15 are foreseen to power the next generation of long range civil aircraft. Advanced integration concepts featuring shape and position optimization allow an efficient overall integration for these large engine types despite the need to realize very close coupling with the wing in order to utilize the increased propulsive efficiency without the need to excessively increase the undercarriage length and thus its weight. The feasibility of efficiently integrating UHBR engines predominantly for design conditions in cruise flight has been investigated and demonstrated over the last decade [1].

Yet, the behavior of UHBR powered engines at the high speed borders of the flight envelope is still widely unknown. Closer coupling to the wing and the enlarged nacelle diameter may change the aerodynamic interference compared to more conventional engine types. Even for these concepts, the available insight at high speed stall conditions is very limited. In order to assess these high speed buffet phenomena and associated engine integration effects, the DFG

*Research Scientist, Institute of Aerodynamics and Flow Technologies, Transport Aircraft Division
†Head of Department, Institute of Aerodynamics and Flow Technologies, Transport Aircraft Division

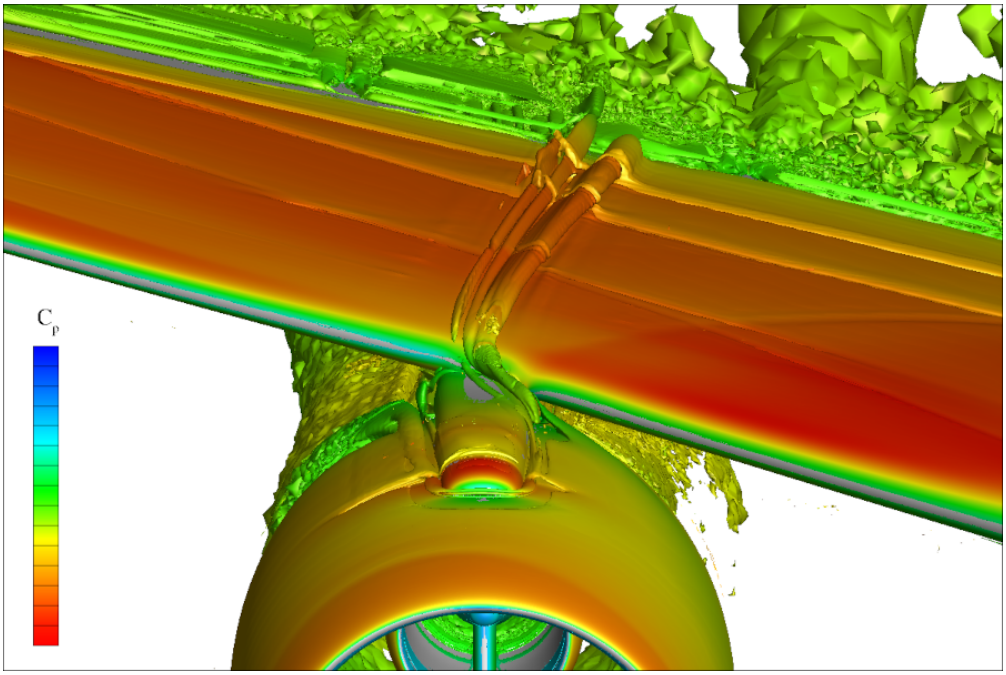

Fig. 1 Vortices originating from nacelle-pylon installation passing over the wing upper surface at $M = 0.84$, $Re = 2.5e07$ at a moderate angle of attack depicted by isosurfaces of Q-criterion at $Q = 1$.

(Deutsche Forschungsgemeinschaft, German Research Foundation) established the research unit FOR 2895 entitled "Unsteady flow and interaction phenomena at High-Speed Stall conditions" in 2020 [2]. The project is dedicated to mature and use hybrid RANS/LES methods to investigate these phenomena with an appropriate level of fidelity. In order to validate these hybrid methods, dedicated wind tunnel experiments funded by the HGF (Helmholtz-Gemeinschaft Deutscher Forschungszentren, Helmholtz Association) are conducted in the ETW facility (European Transonic Wind Tunnel). For this purpose, the XRF1 wind tunnel model was provided by Airbus and has been equipped with two UHBR through flow nacelles designed and integrated by DLR [3]. A unique aspect of these test campaigns were the introduction of PIV (Particle Image Velocimetry) and unsteady PSP (Pressure Sensitive Paint) measurements of buffet phenomena on a transport aircraft model under cryogenic conditions.

First investigations within the FOR 2895 indicated up to now barely considered interference phenomena occurring at high speed conditions. Vortex like structures emerging from the pylon-nacelle intersection where found to be passing over the wing and interacting with the transonic flow field of the wing suction side. An example of such a flow field is shown in Figure 1 depicting vortex like structures visualized by positive Q-criterion originating from the nacelle/pylon assembly and passing over the wing.

Wing suction side vortex interaction is usually encountered in high-lift aerodynamics near stall conditions [4]. The cutout of the high-lift leading edge devices necessary for the installation of underwing engines results in very complex geometrical features producing numerous vortices [5, 6]. If not properly dealt with these vortices result in a significant reduction in maximum lift coefficient having severe adverse effects on overall aircraft performance. A very common approach in the aircraft industry to deal with this kind of problem is the installation of a so called *strake* on the nacelle producing another vortex that stabilizes the boundary layer flow over the wing [4, 7] while other options such as active flow control are investigated as well [8].

While being known in high-lift aerodynamics for quite a while, this kind of phenomenon has not gotten much attention at high speed conditions near cruise. Nevertheless, the ever closer coupling of UHBR nacelles to the wing may require to account for these effects in the future. This paper will give an overview of a first assessment of the phenomena and the implications that come with it.

II. Setup

A. Geometry

The study was performed on the Airbus XRF1 wind tunnel model geometry fitted with newly designed UHBR through flow nacelles. The XRF1 wind tunnel model is representative for a state of the art long range transport aircraft and was designed for high speed wind tunnel testing [9]. The new through flow nacelles were designed by DLR [3] with the intention to provide a state-of-the-art research baseline for high speed off design studies at the border of the flight envelope conducted within the research unit 2895 [2]. Figure 2 shows an overview of the configuration assessed in this study.

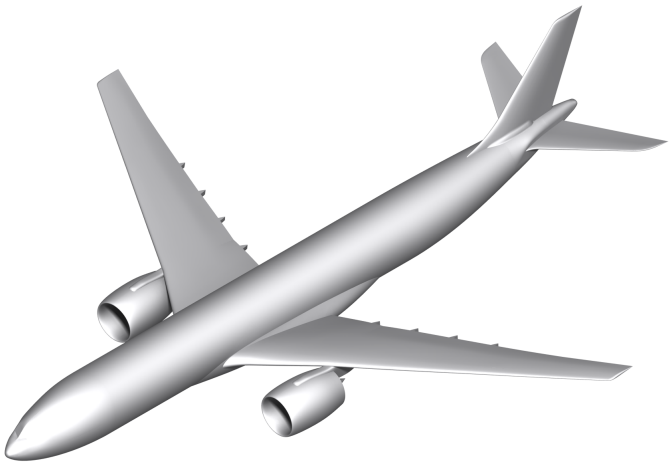

Fig. 2 XRF1 wind tunnel model geometry with UHBR trough flow nacelles.

B. Numerics

The phenomena are investigated by performing steady RANS simulations using the DLR TAU Code [10]. In order to reduce the required computing time a half model of the XRF1 geometry is simulated assuming symmetry of the flow. Turbulence closure is achieved by an SSG/LLR-lnω Reynolds stress turbulence model [11]. More details on turbulence modeling as well as a comparison of the results with a classic eddy viscosity model is presented in Chapter II.C. Spatial discretization of the convective fluxes was realized using a second order central difference scheme with matrix dissipation.

The hybrid unstructured meshes for the numerical simulations were created using *Pointwise*[12]. Special care was taken to accurately resolve the boundary layer flow and shock systems around the wing. The boundary layer part of the meshes consist of structured hexahedra to minimize numerical dissipation and the height of the hexahedra stack normal to the surface was chosen such as to extend over twice the expected boundary layer height. Around the wing upper and lower surface, hexahedra blocks were attached to the boundary layer mesh extending further out to resolve the supersonic flow regions and corresponding shocks. The rest of the volume was then filled with tetrahedra. The total mesh size added up to 1.38×10^8 points. The wing surface is deformed for each M-α combination using measurement data from wind tunnel experiments in order to account for model deformation under load and allowing to compare the results with wind tunnel data. If no steady state solution could be obtained, averaged values of the flow field over the last 2000 timesteps were used to produce the figures.

Throughout the study the Q-criterion [13] is used to identify vortex-like structures within the flow fields. It is defined based on the strain rate tensor S and the vorticity tensor Ω as stated in equation 1. Positive values of Q indicate areas where vorticity is dominant and therefore vortices may be present.

$$Q = \frac{1}{2}(||\Omega||^2 - ||S||^2) \tag{1}$$

C. Turbulence modeling

Special care is taken in terms of turbulence modeling because the corner flow at the intersections of nacelle, pylon and wing is known to be very challenging to predict numerically. Two turbulence models were tested to assess the influence on the development of the pylon-nacelle-wing vortices. The Spalart-Allmaras turbulence model in its negative formulation [14] was used with the QCR extension [15] and a vortical flow correction model [16]. The model is hereafter denoted *SARC-QCR*. The second model applied is the SSG/LRR reynolds stress model [11] relying on a simple gradient diffusion model [17]. The model is hereafter denoted *SSG/LRR-lnω-RSM*.

In Figure 3, a direct comparison of the developing vortex structures at the engine installation position is shown for both turbulence models investigated. Vortex visualization is achieved by plotting surfaces of $Q = 1$ colored by vorticity magnitude. Both turbulence models predict the occurrence of vortex structures originating from the engine installation. The eddy viscosity model as well as the Reynolds stress model predict a horseshoe vortex located where the pylon leading edge intersects the nacelle upper surface. In addition, both models indicate larger vortex structures passing over the wing originating at the position where the pylon intersects the wing leading edge. The structures observed above the wing surface with the Reynolds stress model are much more intricate and detailed compared to those of the eddy viscosity model. The SARC-QCR model in addition indicates a flow separation on the wing upper surface due to the inboard vortex-like structure interacting with the boundary layer and the rear shock. This can be seen by the thickened Q-isosurface on the wing inboard surface towards the rear in Fig. 3a and was confirmed by skin friction lines on the wing surface (not shown here).

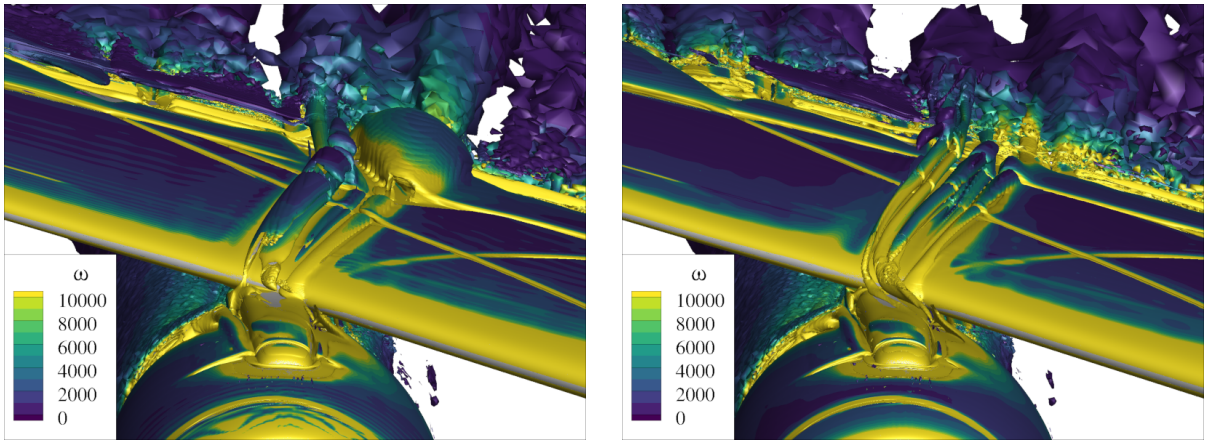

(a) SARC-QCR **(b) SSG/LRR-lnω-RSM**

Fig. 3 Influence of turbulence modeling on the vortex system at $M = 0.84$, $Re = 2.5e07$, $\alpha = 4°$ visualized by isosurfaces of Q-criterion at $Q = 1$.

In Fig. 4 upper wing surface pressure distributions are shown for both turbulence models and for an experimental reference data set obtained from PSP measurements. For details on the PSP measurement technique see Yorita et.al. [18, 19]. The occurrence of a flow separation as predicted by the eddy viscosity model is supported by the upstream shift of the rear shock in the wing pressure distribution in Fig. 4a. This upstream shift of the shock is neither present in the simulation using the Reynolds stress model (Fig. 4b) nor in the experimental reference data (Fig. 4c). Traces of the vortex system are visible in the surface pressure distributions for both turbulence models as well. In order to identify them more easily the area is marked by arrows in Fig. 4. In addition, the range of the color map was narrowed to increase the visibility of the vortex traces. From their starting point the vortex traces run almost perpendicular to the wing leading edge and then slightly curve to the axial direction towards the trailing edge. Indications of these traces can also be identified in the experimental data in the vicinity of the leading edge although being much weaker compared to the simulations.

The findings indicate that the SSG/LRR-lnω-RSM model is best suited for the current study and that the numerical approach is suitable to address the problem at hand. The reason for the RSM model to outperform the eddy viscosity approach is probably linked to the anisotropic nature of the turbulence in the intersection areas of nacelle, pylon and leading edge that can not be displayed by the eddy viscosity model.

(a) SARC-QCR **(b) SSG/LRR-lnω-RSM** **(c) PSP**

Fig. 4 Wing pressure distributions at $M = 0.84$, $Re = 2.5e07$, $\alpha = 4°$

III. Results

In the following an assessment of the observed vortex structures is performed for flow conditions representative of a high speed cruise case followed by an exploration of varying Mach numbers and angles of attack. All simulations were performed with the SSG/LLR-lnω-RSM turbulence model and the numerical settings described in chapter II.B.

A. High Speed Moderate Angle of Attack

Figure 5a shows the evolution of the vortex structure along the nacelle-pylon-wing assembly at high speed conditions for a moderate angle of attack. At the intersection of the pylon with the nacelle a horseshoe vortex is formed marked in blue. The outboard part (in the figure on the left) of the horseshoe vortex passes under the wing and has a clockwise sense of rotation viewing downstream. The inboard part of the horseshoe vortex (V_I) however follows the pylon-nacelle intersection line until the pressure field of the wing leading edge forces it to separate from the nacelle and pass over the pylon and then over the wing suction side. From the x-vorticity the sense of rotation of this vortex can be identified as counter-clockwise looking downstream. The second streamline (V_{II}) in Fig. 5a is found to be a secondary flow induced by the nacelle vortex (V_{III}) originating at the inboard pylon wing intersection . The sense of rotation of V_{III} is clockwise viewed downstream and therefore opposite to V_I. The presence of these vortex structures results in reduced Mach number levels around the wing leading edge as evident from the $M = 1$ isosurface shown in white in Fig. 5b (note that the orange colored regions are contours of surface pressure coefficient). Acceleration to supersonic speeds is hereby moved slightly downstream were the vortices impinge on the $M = 1$ isosurface. The surface pressure contour in Fig. 5b shows a certain range of the local pressure distribution. The contour scale is thereby cutoff below the critical pressure coefficient for the free stream Mach number perpendicular to the leading edge giving indications of supersonic flow across the airfoil. Although the vortices impinge the $M = 1$ isosurface the surface pressure distribution is not significantly influenced by it.

The aforementioned findings are additionally supported by data extracted along the streamlines of V_I to V_{III} presented in Fig. 6. The axial coordinate was hereby normalized with the local chord length of the airfoil, the origin ($x/c = 0$) being located at the wing leading edge. In this coordinate frame the pylon leading edge on the nacelle is located at $x/c \approx -0.5$ and the nacelle leading edge comes to lie at $x/c \approx -0.8$. The streamlines were picked by hand in order to ensure good visualization of the course of the structures. Taking a look at Fig. 6a the inboard part of the horseshoe vortex (V_I) can be seen with very large negative x-vorticity at $x/c = -0.5$ where the pylon intersects the nacelle surface. The vorticity rapidly declines further downstream until the wing leading edge is reached at $x/c = 0$. At this location the nacelle vortex (V_{III}) and a second structure (V_{II}) start with opposing signs in vorticity and therefore sense of rotation. The symmetric behavior of V_{II} and V_{III} and the fact that V_{II} shows significantly reduced vorticity levels compared to the nacelle vortex indicates that V_{II} is in fact a secondary vortex feeding on the nacelle vortex.

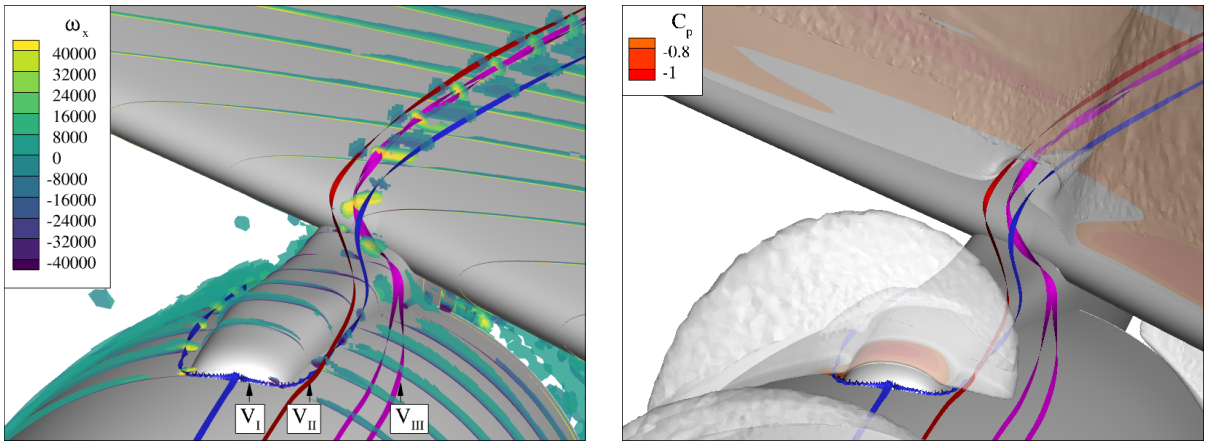

(a) Streamlines and x-vorticity **(b) Streamlines and isosurface of $M = 1$**

Fig. 5 Streamlines of the vortex system at $M = 0.84$, $Re = 2.5e07$, linear range

Overall, the vorticity of this secondary vortex is very weak and comparable to the residuals of the horseshoe vortex. Towards the leading edge at $x/c = 1$ the vorticity of all streamlines has almost vanished.

The extracted Mach number distribution along the streamlines in Fig. 6b proves that the vortex structures are accelerated up to supersonic conditions. The locations where the streamlines pass through the upper surface shock fronts can be identified at 0.25, 0.5 and 0.65 x/c respectively. The first two shocks are thereby oblique shocks and the third shock is a straight one resulting in subsonic conditions downstream (see als Fig. 1). Comparing Fig. 6a and 6b it can be observed that the course of the vorticity of the nacelle vortex (V_{III}) has a kink where the first oblique upper surface shock is located giving an indication of an interaction between a vortex and a shock. From Fig. 5b the impression arises that the pylon horseshoe vortex already reaches supersonic conditions in the vicinity of the pylon leading edge where a small area of supersonic flow is indicated by the $M = 1$ isosurface. Nevertheless, Fig. 6b shows the streamline of V_I remaining subsonic in this region suggesting that the vortex runs inside the boundary layer.

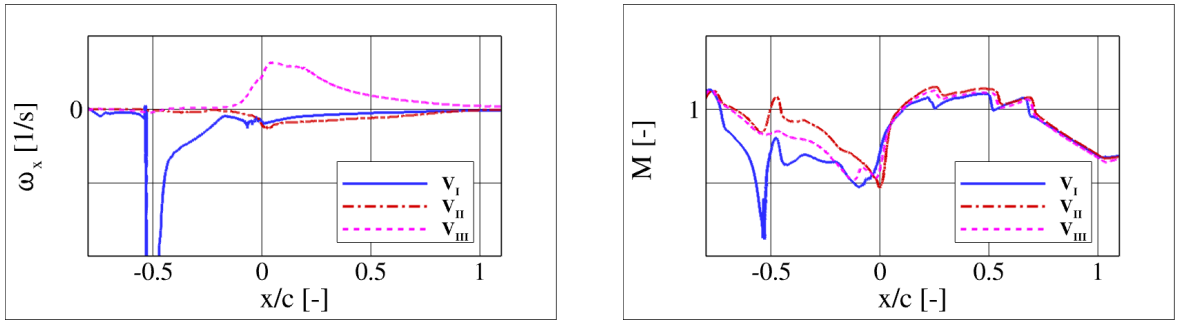

(a) Vorticity **(b) Mach number**

Fig. 6 Variables extracted from streamlines V_I to V_{III} at $M = 0.84$, $Re = 2.5e07$, linear range

B. Mach and Angle of Attack Variation

The numerical study was extended for various angles of attack in order to assess the sensitivity of the vortex system at high speed flight conditions. Figure 7 shows the evolution of the vortex structures depending on the angle of attack for a Mach number of 0.84. Surfaces of positive Q are again used to visualize the vortices. In order to better distinguish the vortices from the edge of the boundary layer, which is inherently visualized by a transition from positive to negative Q as well, contours of the turbulent-laminar viscosity ratio based on turbulence modeling are shown. In the remainder of the chapter, the sense of rotation is discussed various times. For brevity and ease of reading, the sense of rotation is always described as viewing from the front looking downstream.

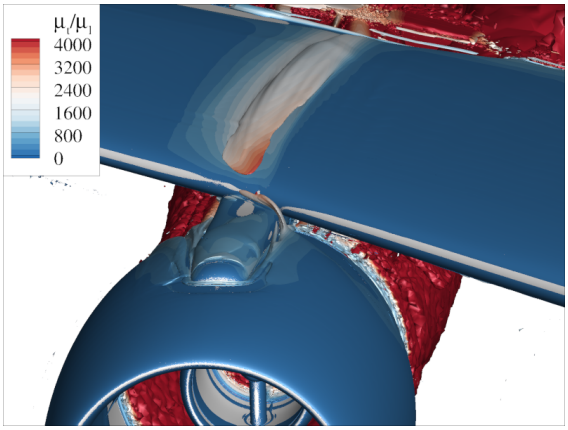

(a) α=-4°

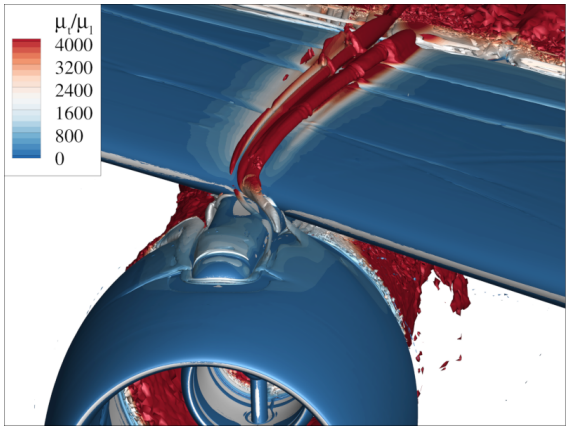

(d) α=2°

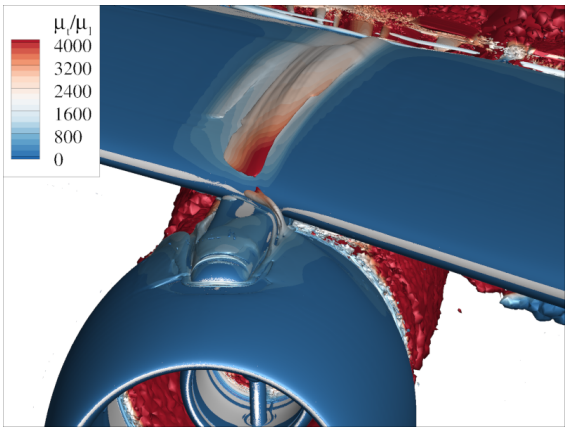

(b) α=-2°

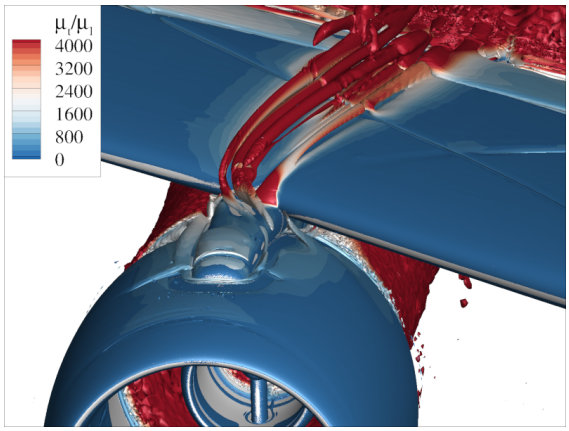

(e) α=4°

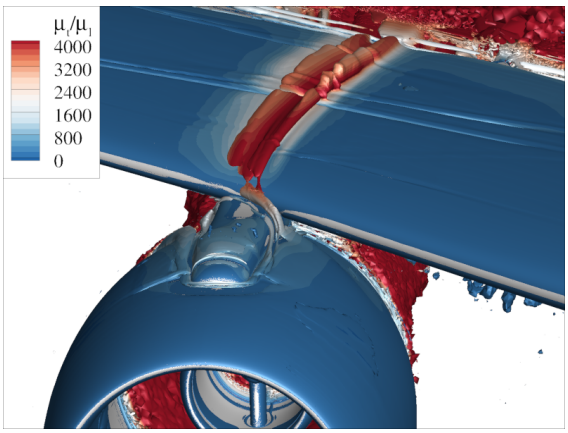

(c) α=0°

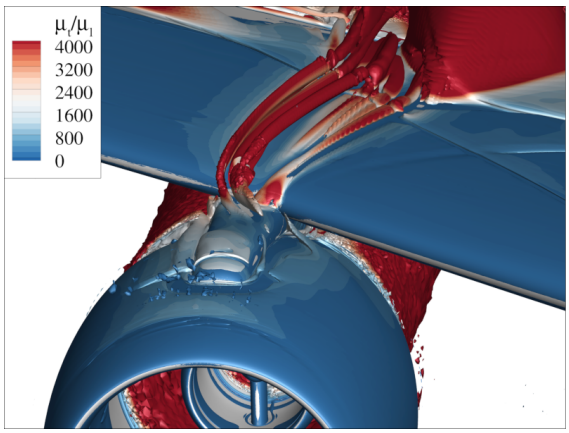

(f) α=5°

Fig. 7 Vortex like structures at $M = 0.84$, $Re = 2.5e07$ visualized by isosurfaces of Q-criterion at $Q = 1$.

For the two lowest angles of attack of -4° and -2°, the Q-criterion shows a flat region downstream of the pylon-wing intersection. Further analysis suggests that this is in fact a shear layer due to induced velocities in spanwise direction but not a vortex or vortex like structure. Nevertheless, the horseshoe vortex in front of the pylon leading edge is already present at these conditions although being much weaker compared to the higher angles of attack. The sense of rotation of the horseshoe vortex is clockwise for the outboard part and counter clockwise for the inboard part. At 0° angle of attack the first vortex structures can be observed above the wing and further analysis shows that the flow indeed makes a full revolution around a vortex core with a clockwise sense of rotation. Although it is difficult to attribute this structure due to it being still very weak at this angle, it is believed that this vortex structure is linked to the nacelle vortex. For $\alpha = 2$ this structure becomes more prominent but remains the same topology. From this angle on a continuous Q-isosurface is visible showing its origin being indeed located on the nacelle rear part close to the inboard pylon intersection. From this it becomes more clear that this is indeed the nacelle vortex. In addition, to the nacelle vortex, secondary flow structures with counter clockwise sense of rotation can be identified as already discussed in section III.A. Starting from angle of attack of 4° the vortex system becomes more complex by the introduction of another structure originating directly at the inboard part of the wing-pylon intersection line. This vortex is located inboard of the previously described vortex system and flows almost parallel to it. Its sense of rotation is counter clockwise and its vorticity is significantly higher compared to the other vortex structures described. Its origin is linked to a corner separation in the pylon wing intersection starting to appear between 2° and 4° angle of attack. Further analysis is required to determine the exact onset angle. No direct interaction between this vortex and the previously described nacelle vortex system is visible at this point. At the highest analyzed angle of attack of 5° this pylon-wing vortex results in a flow separation further downstream where it interacts with the rear shock of the wing similar to what was observed for the eddy viscosity model at a lower angle of attack in chapter II.C. The nacelle vortex system (V_I-V_{III}) remains unaffected by this and is very similar to α at 2° and 4°. In fact, the flow separation can solely be attributed to the pylon wing vortex as described in more detail in section III.C.

The study was further extended by performing simulations at a higher Mach number of 0.9. The results are shown in Fig. 8 for a range of angles of attack ranging from -2° to 6°. The overall behavior of the vortex system is similar to the lower Mach number of 0.84. At the lowest angle of attack of -2° a shallow structure is enveloped by the Q-criterion isosurface above the wing. As previously, this is a structure resulting from shear flow and not a rotating vortex. The pylon horseshoe vortex is likewise present. At α=0° the shear layer rolled up into a small vortex rotating clockwise indicating that this is again the nacelle vortex. As for the lower Mach number case and discussed in section III.A, a secondary structure is visible in Fig. 8b outboard of the primary vortex. Contrary to what was observed for the Mach 0.84 case, the vortex structure associated with the pylon-wing corner separation already appears at an angle of attack of 2° in Fig. 8c. Its course over the wing is parallel to the nacelle vortex and the secondary flow structure without showing any interference with them. Starting from $\alpha = 4$ the pylon-wing corner separation vortex is much stronger compared to the rest of the vortex system as observed for the lower Mach number. At the highest observed angle of attack of 6° this pylon-wing vortex results in a flow separation towards the trailing edge similar to the $M = 0.84$ study. Again, no interference is observed between the pylon-wing vortex and the nacelle vortex system. It can be concluded that the same mechanism is at work for both Mach numbers investigated.

C. Vortex Induced Inboard Stall

In the previous chapter the vortex developing from the corner stall in the pylon-wing intersection showed to be responsible for a local flow separation on the wing inboard of the nacelle towards the trailing edge (see Fig. 7 f). In Fig. 9a the clean configuration of the XRF1 is shown for a Mach number of 0.84 and an angle of attack of 5° without a nacelle attached to prove that this effect is indeed related to the pylon-wing vortex. In Fig. 9 surface contours of negative $c_{f,x}$ indicate flow separations while slices of total pressure blanked at 95% free stream value are intended to give an indication for boundary layer thickness and low total pressure flow. For the clean configuration no inboard flow separation is observed, although the midboard and outboard portion of the wing show significant flow separations. These are associated with shock/boundary layer interactions resulting from the high Mach number and high angle of attack conditions.

A more detailed view on the inboard separation on the wing induced by the pylon-wing vortex is shown in Fig. 9b. The strong negative values of skin friction coefficient in the pylon-wing intersection mark the origin of this vortex. From the slices just downstream of this separation colored by total pressure it can be seen that a large total pressure deficit is present in the flow. Following slices of the pylon-wing vortex downstream it can bee seen that the boundary layer located inboard of the vortex is thickened due to the counter clockwise rotation of the flow. Meanwhile the total pressure deficit in the vortex core partly recovers from a minimum value of $p_t/p_{t,\infty} \approx 0.5$ close to the leading edge to

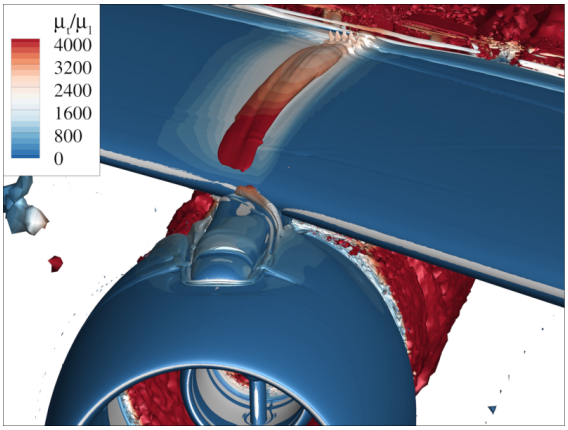

(a) α=-2°

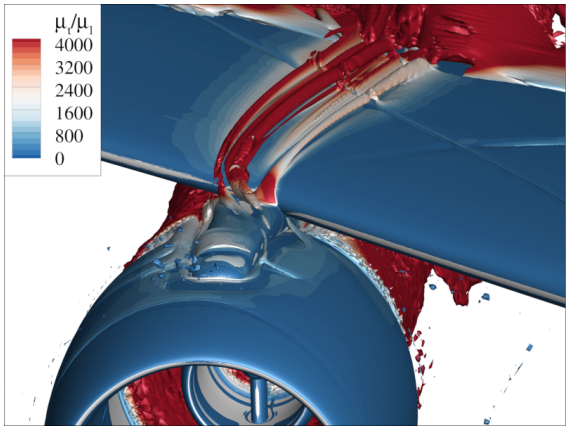

(d) α=4°

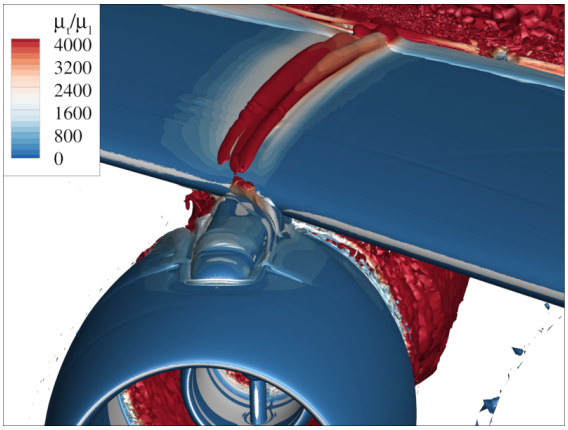

(b) α=0°

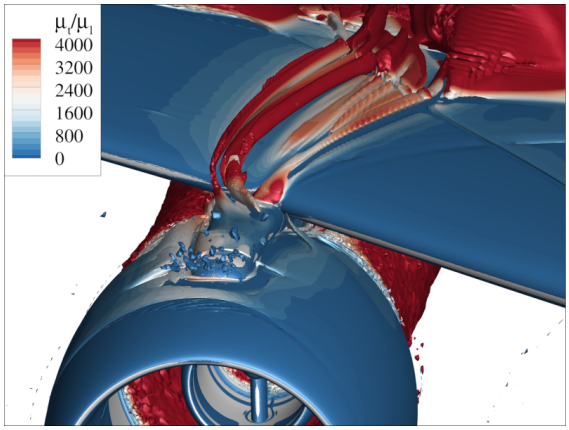

(e) α=6°

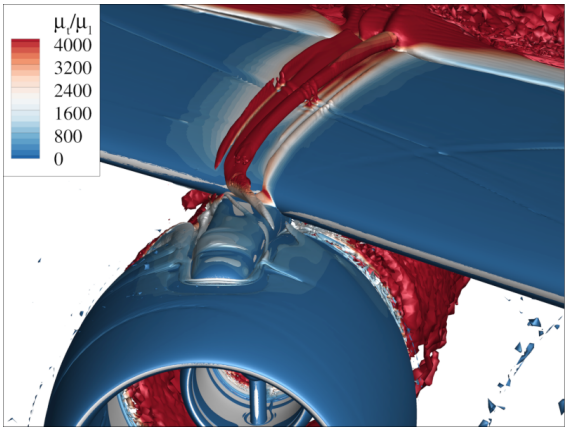

(c) α=2°

Fig. 8 Vortex like structures at $M = 0.90$, $Re = 2.5e07$ visualized by isosurfaces of Q-criterion at $Q = 1$.

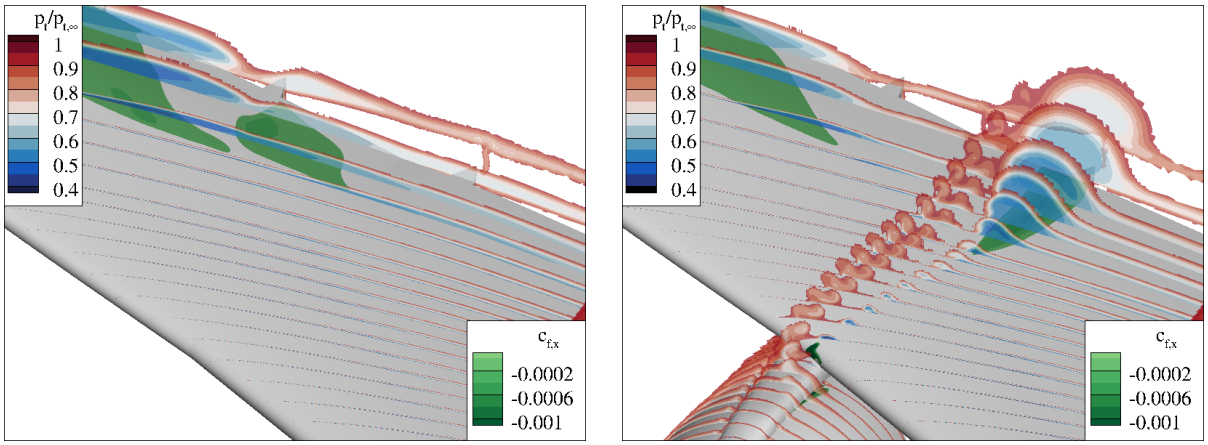

(a) Wing without nacelle **(b) Wing and UHBR**

Fig. 9 Visualization of local flow separation and vortex structures at $M = 0.84$, $Re = 2.5e07$, $\alpha = 5°$.

values of $p_t/p_{t,\infty} \approx 0.7$ just before the burst of the separation. Note that the inboard wing flow separation indicated by the $c_{f,x}$ contour indeed start from the thickened boundary layer and not from the total pressure deficit in the vortex core that is located slightly outboard. From this the conclusion is drawn that the separation is a result of the rotating flow pulling on the boundary layer on its inboard side weakening the latter in the process while the flow located just outboard of the vortex is stabilized due to the additional downwash of the vortex pushing down on the boundary layer. The axial location of the beginning of the flow separation coincides with the position of the straight shock on the wing decelerating the flow to subsonic conditions. The resulting rise in static pressure acts on the locally weakened boundary layer forcing it to separated from the surface. Upon careful inspection locally thickened boundary layers can also be observed for the nacelle vortex system flowing over the wing outboard of the previously discussed pylon-wing vortex. However, the rotation of these vortices is not strong enough to weaken the boundary layer to trigger a flow separation. Therefore the pylon-wing vortex is of primary importance when dealing with vortex related high speed stall.

D. Topology of Identified Vortex System

Summarizing the previously presented results the following vortex system as depicted in Fig. 10 emerges for high speed cruise and high speed stall conditions. For very low angles of attack only the pylon-horseshoe vortex is present whose inboard part is deflected over the wing but does not show any interference with the wing pressure distribution. At moderate angles of attack the nacelle vortex develops. It passes over the inboard part of the pylon-horseshoe vortex in the vicinity of the wing leading edge and flows side by side to it over the wing. Outboard of the nacelle vortex a secondary flow structure with very weak vorticity emerges starting just downstream of the wing leading edge, possibly induced by the rotation of the nacelle vortex. At high angles of attack a corner stall in the pylon-wing intersection results in the pylon-wing vortex. It is stronger compared to the nacelle and pylon-horseshoe vortices and interacts with the wing flow towards the trailing edge resulting in flow separation at high angles of attack. It does not interfere with the other vortices described.

IV. Conclusion

The present study reveals vortices due to the installation of closely coupled UHBR nacelles and their interactions with the upper wing surface under transonic conditions. Such effects were previously found for high-lift aerodynamics and have not gained much attention yet for high speed flows.

Steady RANS simulations were performed to investigate the phenomena. It was found that a Reynolds stress turbulence model is required to accurately resolve the flow features that were subject to the study. The simulations were carried out for various Mach numbers and angles of attack in order to assess the the sensitivity of the vortex systems in the high speed stall regime. The analysis suggests that four different vortex structures are present depending on the local angle of attack. The vortices interact with the transonic flow field above the wing and are being accelerated up to supersonic conditions. At moderate angles of attack the nacelle vortex is the most prominent vortex structure flowing

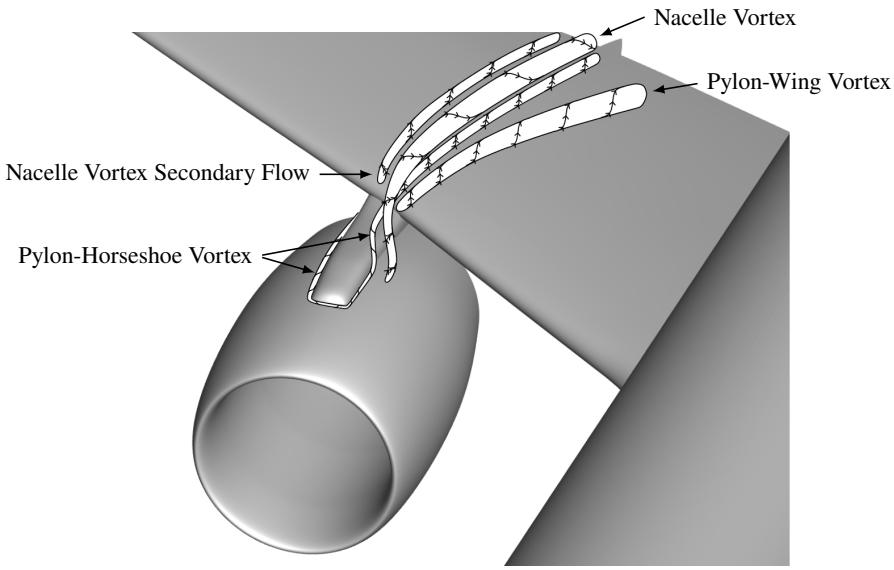

Fig. 10 Wing-Pylon-Nacelle Vortex System.

over the wing. Nevertheless, at these conditions no significant detrimental interaction of the nacelle vortex with the wing flow is observed. At high angles of attack a vortex originating from the pylon-wing intersection area emerges interaction with the transonic flow at the wing trailing edge. This results in a local flow separation downstream of the spanwise engine installation position that contribute to inboard wing stall at high speed high angle of attack conditions. These observations contribute to the intentions of the research unit FOR 2895 as it is dedicated to further enhance the knowledge on high speed stall phenomena.

Future work may include experiments using PIV to confirm the nature of the presented vortex systems and validate the findings. In addition, higher order methods including scale resolving simulations may be suited to gain a deeper insight into the vortex phenomena.

V. Acknowledgement

The authors gratefully acknowledge the Deutsche Forschungsgemeinschaft DFG (German Research Foundation) for funding this work in the framework of the research unit FOR 2895. The authors would like to thank the Helmholtz Gemeinschaft HGF (Helmholtz Association), Deutsches Zentrum für Luft- und Raumfahrt DLR (German Aerospace Center) and Airbus for providing the wind tunnel model and financing the wind tunnel measurements.

References

[1] Magrini, A., Benini, E., Yao, H.-D., Postma, J., and Sheaf, C., "A review of installation effects of ultra-high bypass ratio engines," *Progress in Aerospace Sciences*, Vol. 119, 2020, p. 100680. https://doi.org/10.1016/j.paerosci.2020.100680.

[2] Lutz, T., Kleinert, J., Waldmann, A., Koop, L., Yorita, D., Dietz, G., and Schulz, M., "Research Initiative for Numerical and Experimental Studies on High Speed Stall of Civil Aircraft," *accepted for publication in Journal of Aircraft*, 2022.

[3] Spinner, S., and Rudnik, R., "Design of a UHBR Through Flow Nacelle for High Speed Stall Wind Tunnel Investigations," *Deutscher Luft- und Raumfahrt Kongress 2021*, Deutsche Gesellschaft für Luft- und Raumfahrt - Lilienthal-Oberth e.V., 2021. https://doi.org/10.25967/550043.

[4] Haines, A., "Scale Effects on Aircraft and Weapon Aerodynamics," *AGARD-AD-323*, edited by A. Young, 1994.

[5] von Geyr, H. F., Schade, N., van der Burg, J., Eliasson, P., and Esquieu, S., "CFD Prediciton of Maximum Lift Effects on Realistic High-Lift-Commercial-Aircraft-Configurations within the European project EUROLIFT II," *25th AIAA Applied Aerodynamics Conference*, American Institute of Aeronautics and Astronautics, 2007. https://doi.org/10.2514/6.2007-4299.

[6] Koklu, M., Lin, J. C., Hannon, J. A., Melton, L. P., Andino, M. Y., Paschal, K. B., and Vatsa, V. N., "Investigation of the Nacelle/Pylon Vortex System on the High-Lift Common Research Model," *AIAA Journal*, Vol. 59, No. 9, 2021, pp. 3748–3763. https://doi.org/10.2514/1.j059869.

[7] Schaufele, R., "Applied Aerodynamics at the Douglas Aircraft Company - A Historical Perspective," *37th AIAA Aerospace Sciences Meeting and Exhibit*, Reno, NV, USA, 1999.

[8] Hue, D., François, C., Dandois, J., and Gebhardt, A., "Simulations of an aircraft with constant and pulsed blowing flow control at the engine/wing junction," *Aerospace Science and Technology*, Vol. 69, 2017, pp. 659–673. https://doi.org/10.1016/j.ast.2017.07.031.

[9] Mann, A., Thompson, G., and White, P., "Civil Aircraft Wind Tunnel Feature Rich Testing at the Edge of the Envelope," *54th 3AF International Conference on Applied Aerodynamics*, Paris, France, 2019.

[10] Gerhold, T., "Overview of the Hybrid RANS Code TAU," *MEGAFLOW - Numerical Flow Simulation for Aircraft Design*, edited by N. Kroll and J. K. Fassbender, Springer Berlin Heidelberg, Berlin, Heidelberg, 2005, pp. 81–92.

[11] Eisfeld, B., and Rumsey, C., "Length-Scale Correction for Reynolds-Stress Modeling," *AIAA Journal*, Vol. 58, No. 4, 2020, pp. 1518–1528. https://doi.org/https://doi.org/10.2514/1.J058858.

[12] "Pointwise V18.4 Release 2 ©2021 Cadence Design Systems, Inc." , 2020. URL www.pointwise.com.

[13] Hunt, J., Wray, A., and Moin, P., "Eddies, stream, and convergence zones in turbulent flows," *Center for Turbulence Research Proceedings of the Summer Program*, 1988, pp. 193–208.

[14] Allmaras, S., Johnson, F., and Spalart, P., "Modifications and clarifications for the implementation of the Spalart-Akkmaras turbulence model," *ICCFD7-1902, 7th International Conference on Computational Fluid Dynamics*, Big Island, Hawaii, 2012.

[15] Spalart, P., "Strategies for Turbulence Modelling and Simulation," *International Journal of Heat and Fluid Flow*, Vol. 21, 2000, pp. 252–263.

[16] Shur, M., Strelets, M., Travin, A., and Spalart, P., "Turbulence Modeling in Rotating and Curved Channels: Assessing the Spalart-Shur Correction," *AIAA Journal*, Vol. 38, No. 5, 2000, pp. 784–792.

[17] Eisfeld, B., "Implementation of Reynolds Stress Models into the DLR-FLOWer Code," techreport DLR-IB 124-2004/31, Institute of Aerodynamics anf Flow Technologies, DLR, 2004.

[18] Yorita, D., Klein, C., Henne, U., Ondrus, V., Beifuss, U., Hensch, A.-K., Longo, R., Guntermann, P., and Quest, J., "Successful Application of Cryogenic Pressure Sensitive Paint Technique at ETW," *2018 AIAA Aerospace Sciences Meeting*, American Institute of Aeronautics and Astronautics, 2018. https://doi.org/10.2514/6.2018-1136.

[19] Yorita, D., Henne, U., and Klein, C., "Time-resolved Pressure Sensitive Paint Measurements for Cryogenic Wind Tunnel Tests," *submitted for publication in CEAS Aeronautical Journal*, 2022.